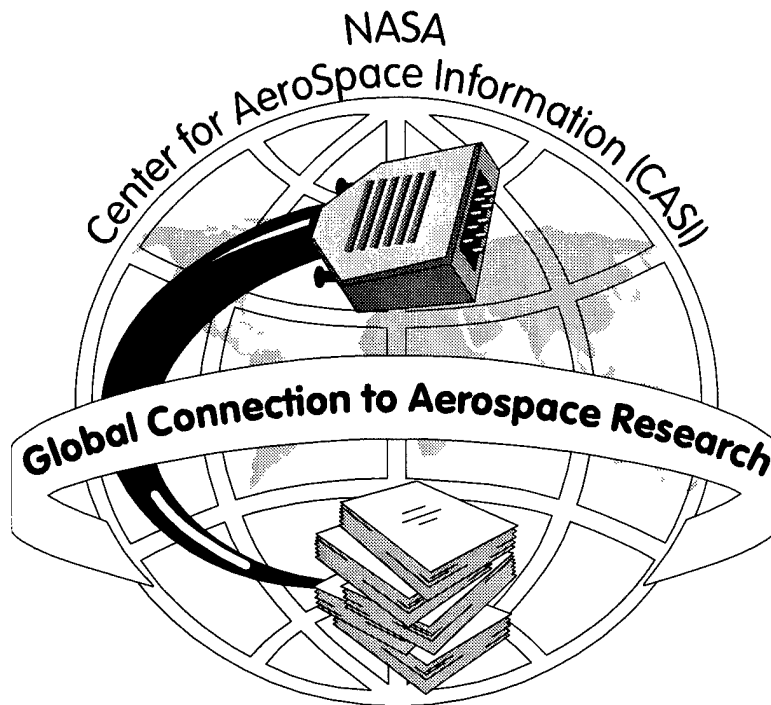


19990028453



A Service of:
National Aeronautics and
Space Administration

20000718 083

DTIC QUALITY INSPECTED 4



SCIENTIFIC &
TECHNICAL INFORMATION

1N-44
-734 827

A Solar Thermophotovoltaic Electric Generator for Remote Power Applications

**NAS3-97047
Final Report**

Contractor –
Essential Research, Inc.
23811 Chagrin Blvd.
Suite 280
Cleveland, OH 44122

ESSENTIAL
RESEARCH
INCORPORATED



Authored by –
Navid S. Fatemi

December 14, 1998

DISTRIBUTION STATEMENT A
Approved for Public Release
Distribution Unlimited

A Solar Thermophotovoltaic Electric Generator for Remote Power Applications

Table of Contents

1.	Background	4
2.	Experimental Procedures	5
2.1.	Monolithic Integrated Module (MIM) Growth and Fabrication.....	5
2.2.	Large-Area MIM Device Fabrication	7
2.3.	MIM Array Fabrication Procedure.....	7
2.4.	Set up Procedure and Testing of MIM Arrays with the Stirling Dish Solar Concentrator	8
2.5.	MIM Performance Calculations Procedure.....	12
3.	Results	15
3.1.	Monolithic Integrated Module (MIM) Device Performance.....	15
3.1.1.	Quantum Efficiency (QE) Data.....	15
3.1.2.	High-Level light Illumination I-V Data for MIM Devices	16
3.1.3.	Back Surface Reflector (BSR) Reflectivity Data.....	22
3.2.	MIM Array High-Level light Illumination I-V Data.....	23
3.3.	MIM Array Testing with the Stirling Dish Solar Concentrator.....	25
3.4.	Large-Area MIM Performance Results.....	28
3.5.	Metal-MIM Contact Resistivity Mechanism.....	29
4.	Summary	32
5.	References	32

1. Background

Remote power generation is an important technology for space-based missions and military ground operations. Currently, thermopiles, driven by radioisotope heat sources, are used in deep-space exploration. However, NASA desires to replace this technology because of the perceived environmental threat. In military operations, thermionic or diesel generators are used to provide power. Thermionic generators are inefficient and costly to operate. Particularly when the cost of transporting fuel is high, the use of thermionic generators results in very expensive power.

Thermophotovoltaic (TPV) energy conversion is a technology well suited for the development of highly efficient, compact, and reliable sources of electricity. In TPV energy conversion, heat is first converted to radiant energy by a selective emitter, then to electrical energy by a photovoltaic (PV) cell. For optimal efficiency, the PV cell must have a narrower bandgap than the traditional Si and GaAs cells used for converting the solar spectrum. Currently, TPV systems are under development, utilizing radioisotope and gaseous or liquid combustion heat sources. These approaches have their drawbacks, including (1) the environmental hazard of nuclear materials, (2) the production of NO_x emissions, (3) the consumption of nonrenewable energy, (4) a limited duration of power production, (5) the production of soot, which potentially degrades system performance, and (6) the need for extensive advances in combustor technology to achieve safe, reliable, and compact heat sources.

Solar TPV power generation uses concentrated sunlight as the heat source for TPV conversion. The sun is concentrated and used to heat a thermal absorber. Thermal radiation, and not the solar spectrum, is then converted to electricity with a narrow bandgap PV cell. This concept has been pioneered at McDonnell Douglas Aerospace, who have shown that solar-heated TPV has great potential for supplying large amounts of electricity to the utilities.¹ In addition to efficient energy conversion, solar TPV offers the element of energy storage; power can be produced after sun down, during cloud cover, or continuously during space orbit. Although originally conceived of for commercial application and capable of supplying kilowatts of electricity, solar TPV can easily be scaled down to produce tens or hundreds of watts as needed in mobile or remote power generation. Likewise, it has a high power-to-mass ratio and can thus be configured for use in space exploration.

The use of concentrated solar energy as a heat source does not have the drawbacks associated with radioisotope or combustion heat sources. A very pragmatic advantage of solar power is that dish concentrators are a well-developed technology. Therefore, the development effort and time to market, relative to other TPV concepts, will be reduced. It is the only TPV approach based upon a renewable energy source. In addition, solar TPV has no moving parts, is lightweight, and produces no noise or vibration. It has the potential to be extremely reliable.

Solar TPV is projected to be cost-competitive with traditional means of photovoltaic power generation for supplying large amounts of power to utilities. The McDonnell Douglas study projects that solar TPV will be both more efficient, and less costly to operate, than the Kinematics Stirling Dish. It has the potential to greatly reduce the cost of remote power generation for some military operations. When scaled down for remote applications, solar TPV is expected to be at least twice as efficient as thermionic generators. For deep space exploration, solar TPV may be the only practical replacement to

radioisotope heat sources. Even with a large thermal storage system capable of maintaining constant power output during the orbit night, the mass would be less than a space solar dynamic system. The solar TPV system can also be shielded to eliminate degradation due to radiation. With no moving parts, solar TPV offers the high reliability required for space operation and the low operating and maintenance cost required for utility operation.

2. Experimental Procedures

2.1. Monolithic Integrated Module (MIM) Growth and Fabrication

A fast switching, horizontal, low-pressure OMVPE reactor was employed for all semiconductor material growth. The reactant species were trimethylindium (TMIn), trimethylgallium (TMGa), diethylzinc (DEZn), phosphine (PH₃), arsine (AsH₃) and silane (SiH₄). Hydrogen carrier gas was used to inject the precursors into the reaction chamber. Samples were characterized for crystal quality, alloy composition, and surface morphology using high-resolution double-crystal x-ray diffraction (HRXRD), visual observations, and Normarski contrast optical microscopy.

In_xGa_{1-x}As layers were grown on semi-insulating (S.I.) InP wafers, which were prepared by the substrate vendor (Sumitomo Corp.). A thin layer of InP was first grown on all substrates to provide a clean surface for nucleation of the InGaAs alloys. Lattice-matched InGaAs structures with E_g = 0.74 eV were grown on the InP nucleation layer. All cell structures were capped with an InP window 0.10 μm thick. An InGaAs contact layer was also grown on top of the InP window to provide for the deposition of low contact resistivity metallization. Growth temperature and pressure were 620° C and 190 torr respectively, throughout all OMVPE runs. A schematic cross-section of a complete MIM structure is shown in Figure 1. Each individual cell within a MIM had an area of approximately 0.0552 cm².

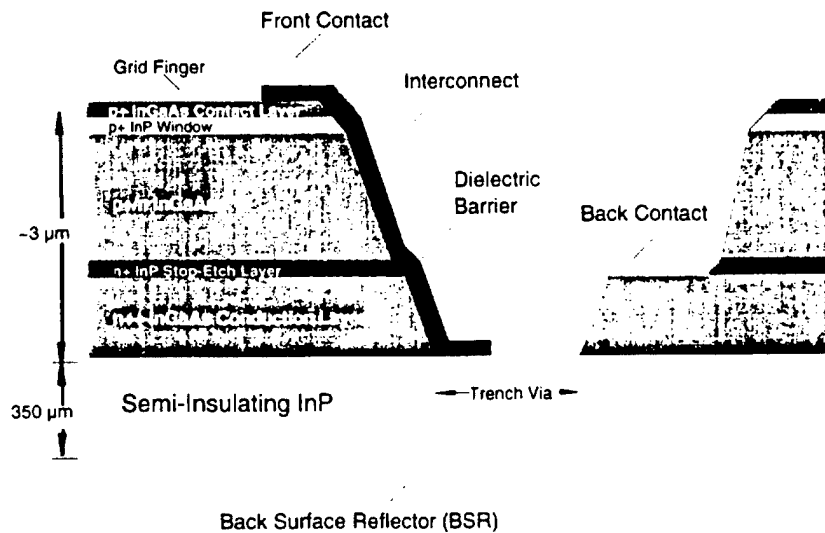


Figure 1.—Schematic cross-section of a MIM structure with E_g = 0.74 eV.

The OMVPE grown cell structures were then processed into MIMs. Five steps of photolithography, two etching steps, one dielectric spin-on and curing step, two metallization steps, and one anti-reflection (AR) coating step were used to fabricate individual MIM devices. Front, back, and interconnect metallization steps were carried out by sequential deposition of Cr (450 Å) and Au (~3 μm). The back surface reflector (BSR) was a gold layer of ~3 μm thickness. The double-layer anti-reflection coating was sequentially deposited ZnS (1400 Å) and MgF₂ (2300 Å). A planar view schematic and photograph of a MIM are shown in Figure 2.

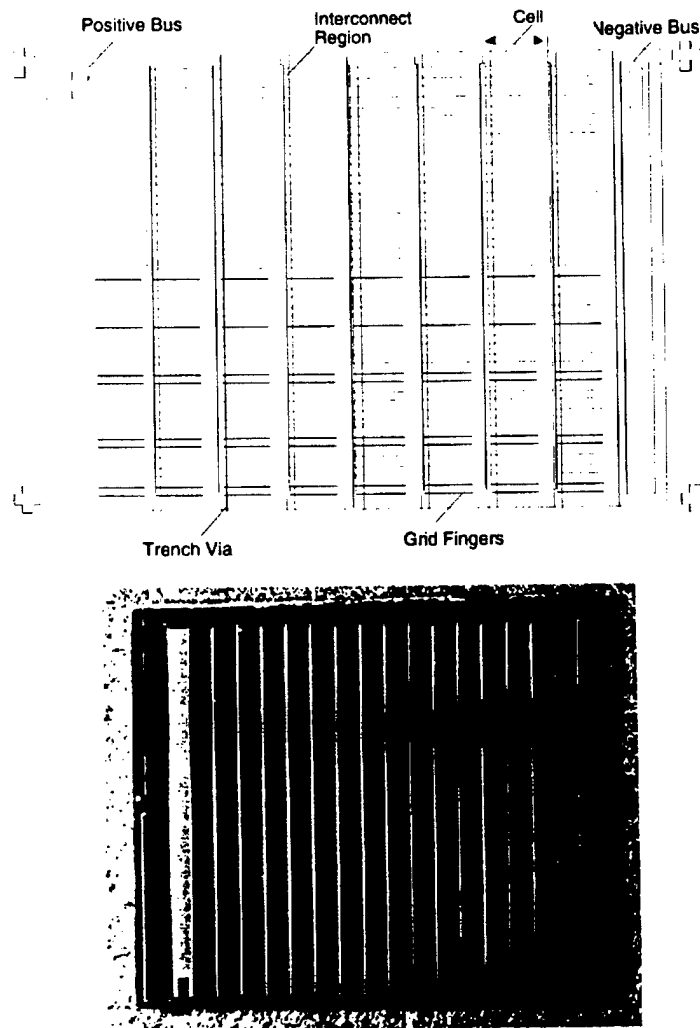


Figure 2.—Schematic planar view of fabricated MIM (top), and a photograph of a 1x1-cm MIM (bottom).

In addition, several transmission line model (TLM) test pads were fabricated in close proximity to the PV cells. TLM test pads furnished important electrical data about the ohmic contact metallization and the p⁺/n⁺ InP/InGaAs cell emitter, such as metal-semiconductor specific contact resistivity (ρ_C) and the semiconductor emitter sheet resistivity (R_{sh}). The as-fabricated ρ_C values for the Cr-Au contacts were measured in the range of low 10^{-6} to low 10^{-8} $\Omega\text{-cm}^2$.

2.2. Large-Area MIM Device Fabrication

The MIM devices that were grown and fabricated for this project mostly had an area of 1 cm^2 (i.e., $1 \times 1\text{-cm}$). However, Large-scale commercialization of the MIMs is expected to require the growth and fabrication of larger area MIMs. We designed a MIM with an area of 4 cm^2 (i.e., $2 \times 2\text{-cm}$) to investigate the feasibility of fabricating larger-area MIMs. This MIM had 30 cells monolithically interconnected in series. A set of photomasks was designed to accommodate one $2 \times 2\text{-cm}$ and seven $1 \times 1\text{-cm}$ MIMs on a 2-inch diameter wafer. Other diagnostic devices such as TLM pads and quantum efficiency diodes were also added to the design. A photograph of a 2-inch diameter wafer with these MIMs is shown in Figure 3.

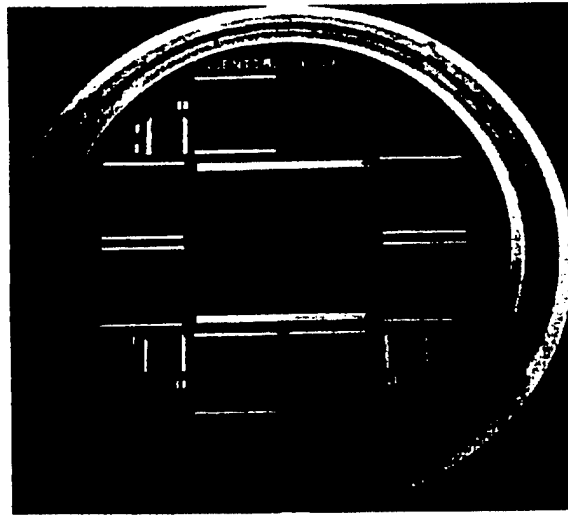


Figure 3.—Photograph of a 2-inch diameter semi-insulating InP wafer with one 30-cell ($2 \times 2\text{-cm}$) and seven 15-cell ($1 \times 1\text{-cm}$) MIMs.

The $1 \times 1\text{-cm}$ and $2 \times 2\text{-cm}$ MIM designs had 15 and 30 cells interconnected in series, respectively. Each individual cell was approximately $550 \mu\text{m}$ wide and either 1 or 2 cm long. Several $2 \times 2\text{-cm}$ MIMs were grown, fabricated, and tested. The test results are given in later sections of this report.

2.3. MIM Array Fabrication Procedure

Six individual $1 \times 1\text{-cm}$ 15-cell MIMs were connected in series to form a string. Two strings were then connected in parallel to form an array. The MIMs were glued to a specially designed water-cooled heatsink. The brass body of the heatsink was soldered to a copper plate for efficient heat transfer. The MIMs were mounted onto the copper plate by a thermally conductive ceramic-filled double-sided adhesive transfer tape, purchased from 3M (model 9882). This tape has a thermal conductivity of 0.43 W/m-K (or $0.25 \text{ BTU/ft. hr. } ^\circ\text{F}$).

A schematic representation of the heatsink is shown in Figure 4.

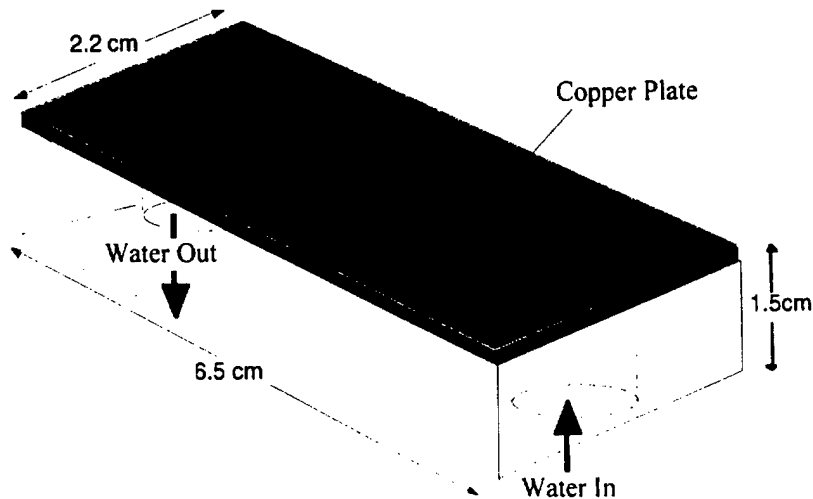


Figure 4.—Schematic of the heatsink.

A gold ribbon of $1\ \mu\text{m}$ thickness and $60\ \mu\text{m}$ width was used to interconnect the negative and positive busbars (both located on the top side) of individual MIMs. A pulsed arc welder was used to fuse the gold ribbon interconnects to the gold metallization of the busbars.

2.4. Set up Procedure and Testing of MIM Arrays with the Stirling Dish Solar Concentrator

The Stirling dish solar concentrator facility at Boeing in Huntington Beach, CA consists of an $\sim 10\text{-m}$ diameter reflective dish with 82 mirror segments. Each segment is approximately one square meter. The segments can be articulated so that the beam power can be focused onto a 6-inch diameter aperture. The receiver for the dish has been described in detail in earlier reports and will only be briefly described here. It consists of a 12-inch diameter alumina cylinder open at one end, for receiving the solar radiation and at the other end is a 10-inch diameter, silicon carbide (SiC) emitter plate. The cylinder is placed inside a 22 inch diameter galvanized steel can with alumina board and fibrous alumina thermal insulation. On the outside of the cylinder, the TPV MIM array is placed approximately 2 cm away from the SiC surface. A schematic of the receiver is shown in Figure 5.

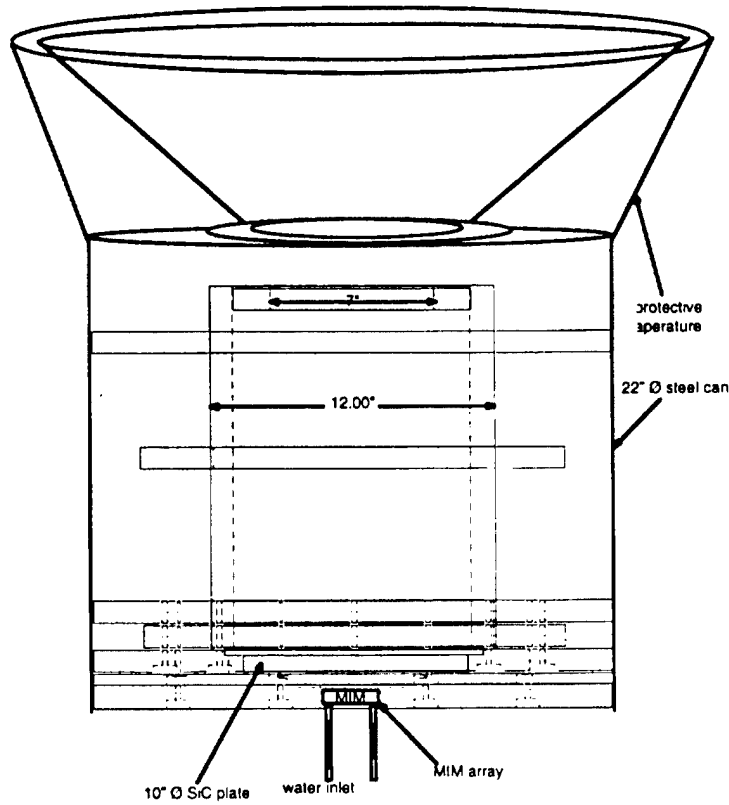


Figure 5.—Schematic cross-section view of the TPV receiver.

The SiC emitter was instrumented with five type-B thermocouples (TCs), four in a compass rose configuration and one near the emitter edge as shown in Figure 6. The TCs were read using a microvolt data logger located inside a “command trailer” approximately 150 feet away. The offset and noise of the data logger was less than $0.01 \mu\text{V}$. The temperature was calculated using thermocouple tables. Reference junctions were not used due to the extremely low noise and offsets.

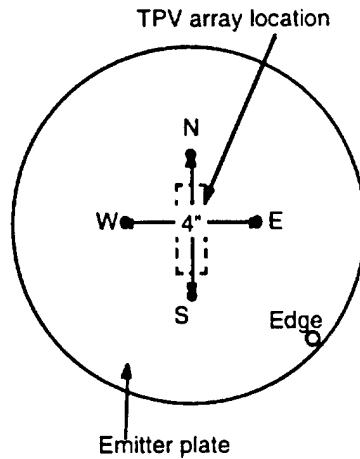


Figure 6.—Location of thermocouples relative to the position of the MIM array.

The receiver assembly was hoisted on to the dish and held in place with C-clamps (Figure 7). On September 24, 1998 the dish was pointed at the sun and the receiver was heated without the MIMs to "ring out" any problems with the SiC emitter before exposing the MIMs to the high temperature conditions. At the beginning of the experiment, only 5 mirror segments were used. Five other segments were sequentially uncovered during the test. All 10 segments had been focused on the emitter by the end of the test. During this test the emitter temperature reached a high of 1280°C on the "West" TC and 1081°C on the edge. The entire emitter was "on sun" for approximately 3 hours. After the test the receiver was inspected visually for damage. The only visible change was a crack in the outer most piece of the alumina insulation. The crack did not have a noticeable effect on mechanical or thermal properties of the receiver in subsequent tests.



Figure 6.—TPV Receiver being mounted to the solar concentrator.

On September 25, 1998 the Receiver and MIM strings were tested together. Before the test, two more mirror facets were uncovered and the other 10 segments were washed. The MIM strings, shown in Figure 8, were cooled with a water flow of ~1.3 gallons per minute (GPM) with an inlet temperature of ~23°C. Each string had a four-wire connection for measuring I-V curves. The electrical connections were routed into the command trailer. The I-V curves were generated using a Keithley current source meter, controlled by a laptop computer. Forty-five I-V curves were generated during a two-hour test. A photograph of the strings in front of the emitter is shown in Figure 9.

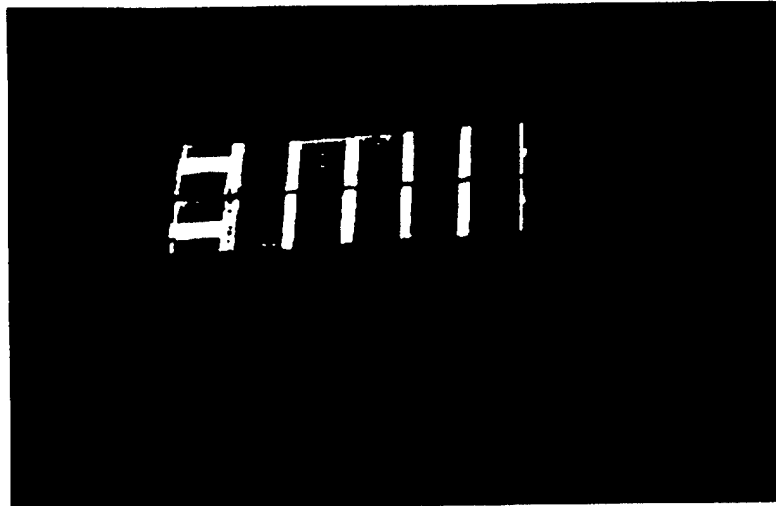


Figure 8.—MIM strings after being tested in front of the emitter.



Figure 9.—MIM strings mounted in front of the emitter plate.

2.5. MIM Performance Calculations Procedure

Figure 10 is a schematic illustration of the TPV process involving MIM with a back surface reflector (BSR). A methodology described below, was used to calculate output current density, output power density, and efficiency values.

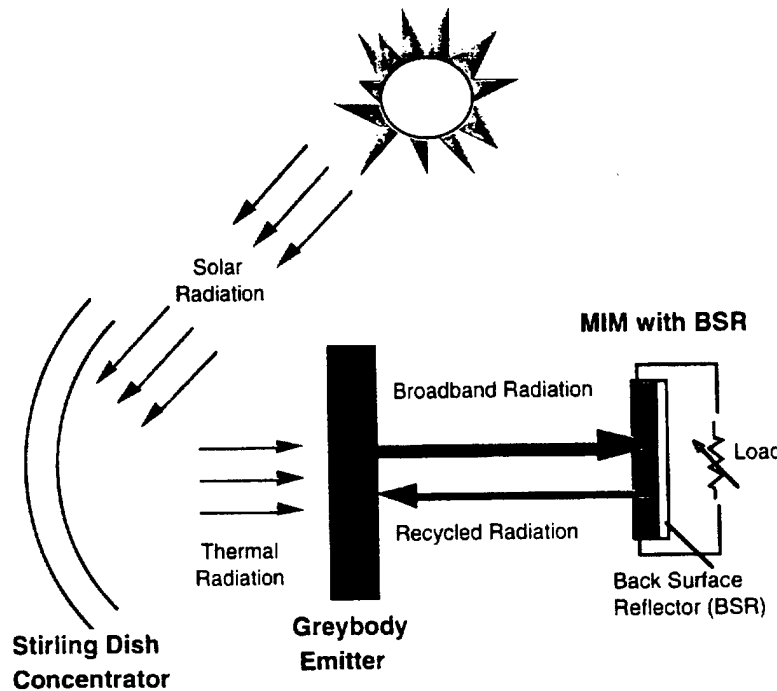


Figure 10.—Schematic representation of the TPV process with MIM.

The output current density (A/cm^2) of the MIMs was calculated by integrating the product of the measured device spectral response ($A/(\mu m \cdot W)$) and the spectral irradiance ($W/(\mu m \cdot cm^2)$) of a graybody (at 1500 K) over all relevant wavelengths. The open-circuit voltage (V_{oc}) and fill factor (FF) values of the MIMs were measured at the output short-circuit current (I_{sc}) levels calculated above, by testing the cells under high-level light concentrations, using a large-area pulsed solar simulator (LAPSS). This technique ensured accurate V_{oc} and FF measurements because the detrimental effects of cell series resistance were experimentally taken into account. The cell output power density (W/cm^2) was then simply calculated as the product of V_{oc} , I_{sc} , and FF.

In order to calculate the in-band efficiency, the MIM output power density calculated above was divided by the total graybody emitter spectral irradiance, integrated to the wavelength of the MIM bandedge (*i.e.*, $1.65 \mu m$). The Excel 5.0 program was used to model, as well as to perform matrix calculations to obtain the desired results. The parameters, symbols, and definitions used for this program are presented in Worksheet I.

Worksheet I.—Parameters used for TPV converter calculations.

System-level Inputs

Variable	Description	Units	Notes
Psys	power output, total system	W	
Top	operating temperature	K	
GFF	geometric focusing factor	dimensionless	=A array/A emitter

System-level Calculated Outputs

Variable	Description	Units	Equation
η_{TPV}	efficiency, TPV converter	dimensionless	$=P_{emitter}/P_{sys}$

Absorber Inputs

Variable	Description	Units	Notes
Absorber	type	text	
Spec _{absorb}	specification	text	
ϵ_{absorb}	emissivity	dimensionless	blackbody

Absorber Calculated Outputs

Variable	Description	Units	Equation
$e_{absorb}(\lambda)$	emissive power	W/($\mu\text{m cm}^2$)	$=\epsilon_{absorb} * C_1/\lambda^5 * (1/\exp(C_2/\lambda T_{op}-1))$
q _{absorb}	total emissive power	W/cm ²	$=\int e_{absorb}(\lambda) \partial\lambda$
P _{absorb}	total emitted power	W	$=q_{absorb} * A_{absorb}$
$e_{emitter}(\lambda)$	emissive power	W/($\mu\text{m cm}^2$)	$=e_{absorb}(\lambda)$
q _{emitter}	total emissive power	W/cm ²	$=q_{absorb}$
P _{emitter}	total emitted power	W	$=P_{absorb}$
A _{absorb}	area	cm ²	$=A_{emitter}$
A _{emitter}	area	cm ²	$=A_{array}/GFF$

Filter Inputs

Variable	Description	Units	Notes
Filter	type	text	
Spec _{filter}	specification	text	
A _{filter}	area	cm ²	
T _{filter} (λ)	transmission	dimensionless	
R _{filter} (λ)	reflection	dimensionless	

Filter Calculated Outputs

Variable	Description	Units	Equation
a _{filter} (λ)	absorption	dimensionless	= 1 - T _{filter} (λ) - R _{filter} (λ)
e _{into_cell} (λ)	emissive power	W/(μm cm ²)	= e _{emitter} (λ) * T _{filter} (λ)

PV Cell Inputs

Variable	Description	Units	Notes
Cell	type	text	
Spec _{cell}	specification	text	
E _g	bandgap	eV	
A _{cell}	area	cm ²	
W _{cell}	weight	g	
T _{cell}	temperature	K	
SR _{cell} (λ)	spectral response	A/(μm W)	
V _{oc}	open-circuit voltage	V	
FF	fill factor	dimensionless	
GSF	grid shadowing factor	dimensionless	
PF	packing factor (cell-array)	dimensionless	

PV Cell Calculated Outputs

Variable	Description	Units	Equation
J _{sc}	short-circuit current density	A/cm ²	= ∫ (SR _{cell} (λ) * e _{into_cell} (λ)) ∂λ [from 0-2 μm]
J _{sc_arc}	short-circuit current density w/AR coat	A/cm ²	= J _{sc} * 1.35
q _{cell}	power-output density	W/cm ²	= J _{sc_arc} * V _{oc} * FF
N _{cell}	number of cells	dimensionless	= int (P _{sys} / (q _{cell} * A _{cell} * GSF) + 1)
A _{array}	area, array	cm ²	= N _{cell} * A _{cell} * PF

3. Results

3.1. Monolithic Integrated Module (MIM) Device Performance

Several growth runs were carried out to fabricate lattice-matched InGaAs monolithic integrated module (MIM) photovoltaic (PV) devices on InP, with a bandgap (E_g) 0.74 eV. The current-voltage (I-V) characteristics of each cell were initially tested under air-mass zero (AM0) conditions. Quantum efficiency measurements were then performed so that the results could be used in output power density calculations (See Section 3.5). These measurements also served as diagnostic tools to evaluate device quality. Finally, the MIMs were tested under high-level light illumination using a large-area pulsed solar simulator (LAPSS) system to assess their anticipated electrical performance under the intended TPV operating conditions. The details of the results of these measurements are presented below.

3.1.1. Quantum Efficiency (QE) Data

Quantum efficiency (QE) of every MIM growth run was measured after the application of the anti-reflection (AR) coating. The results were very similar for every growth run. An example of a typical QE plot for a MIM is given in Figure 11.

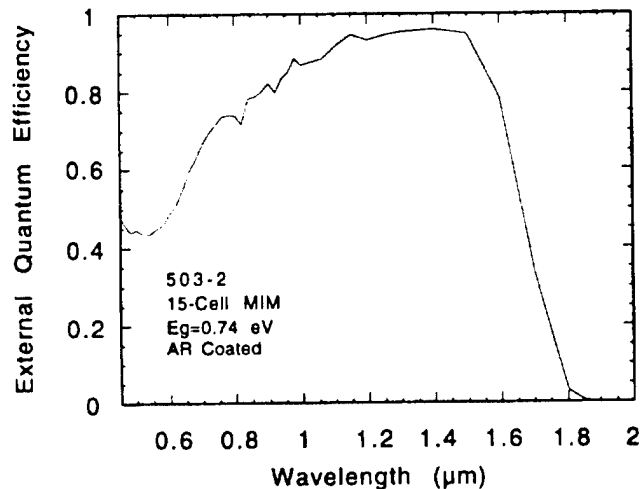


Figure 11.—Measured External quantum efficiency of a MIM with $E_g = 0.74$ eV.

As shown in the figure, excellent minority carrier collection efficiency (near unity) was observed with these MIMs. The data presented in the above figure was also used to make theoretical projections on the device performance under TPV conditions.

3.1.2. High-Level light Illumination I-V Data for MIM Devices

LAPSS testing was performed on all individual MIMs used to fabricate the MIM arrays. From these measurements, diode ideality factor (A), reverse saturation current density (J_0), and the effects of the series resistance on device FF were determined. The light concentration levels were chosen such that the J_{sc} of each device would be in the same range as the anticipated J_{sc} when operating under TPV conditions. The results for some of the measurements including maximum power (P_{max}) and efficiency (η) are shown in Tables II-VII.

Table II.—High illumination I-V data (25 °C) for 15-cell (1x1 cm) MIMs with $E_g = 0.74$ eV (Run 470).

Cell I.D.	Isc (mA)	Voc (mV)	FF (%)	P_{max} (mW)	AM0 η (%)	Comments
						No ARC
470-4	2.67	5094	72.7	9.89	8.04	0.1/1.0 μm emitt/LCL
	174	6971	71.2	864		@3.16 A/cm ²
	230	7088	69.6	1135		@4.17 A/cm ²
-5	2.64	5252	70.6	9.78	7.94	
	231	7060	70.5	1152		@4.19 A/cm ²
-6	2.54	4915	69.5	8.66	7.05	
	225	6933	69.1	1079		@4.08 A/cm ²
-7	2.54	4872	70.0	8.67	7.03	
	226	6968	69.0	1087		@4.09 A/cm ²

Table III.— High illumination I-V data (25 °C) for 15-cell (1x1 cm) MIMs with $E_g = 0.74$ eV (Run 497).

Cell I.D.	Isc (mA)	Voc (mV)	FF (%)	Pmax (mW)	AM0_(%)	Comments
						No ARC
497-1	2.28	4573	69.0	7.18	5.83	0.3/1.0 μm emit/LCL
	194	6666	71.5	926		@3.52 A/ cm^2
-2	2.20	4573	72.0	7.23	5.87	
	186	6510	71.4	866		@3.37 A/ cm^2
-5	2.24	4667	70.9	7.41	6.02	
	191	6691	72.6	928		@3.46 A/ cm^2
-6	2.25	4715	71.0	7.53	6.12	
	193	6695	73.6	952		@3.50 A/ cm^2
-9	2.20	4914	72.8	7.87	6.39	
	186	6703	74.9	933		@3.38 A/ cm^2
	228	6762	74.9	1150		@4.12 A/ cm^2
	268	6841	73.6	1350		@4.86 A/ cm^2
-10	2.23	4937	71.2	7.83	6.36	
	191	6757	74.9	967		@3.46 A/ cm^2
-11	2.18	4710	72.2	7.43	6.03	
	187	6793	73.0	925		@3.39 A/ cm^2
-12	2.11	4717	70.5	7.01	5.69	
	180	6710	74.9	906		@3.26 A/ cm^2

Table IV.— High illumination I-V data (25 °C) for 15-cell (1x1 cm) MIMs with $E_g = 0.74$ eV (Run 500).

Cell I.D.	Isc (mA)	Voc (mV)	FF (%)	Pmax (mW)	AM0 η (%)	Comments
						No ARC
500-1	2.3	4024	63.8	5.8	4.7	0.3/1.0 μm emitt/LCL
	196	6520	69.6	888		@3.54 A/cm ²
-4	2.3	4158	60.1	5.8	4.7	
	203	6541	69.5	923		@3.68 A/cm ²
-5	2.3	4244	66.2	6.4	5.2	
	199	6538	70.7	919		@3.61 A/cm ²
-6	2.4	4905	68.7	7.9	6.5	
	204	6673	74.1	1002		@3.70 A/cm ²
-7	2.3	4579	72.0	7.7	6.3	
	199	6655	72.4	958		@3.61 A/cm ²
-8	2.3	4780	71.6	7.7	6.3	
	198	6595	74.3	968		@3.59 A/cm ²
-9	2.2	4718	67.4	7.1	5.8	
	197	6595	74.2	964		@3.57 A/cm ²
-10	2.3	4852	66.0	7.4	6.0	
	195	6698	67.4	881		@3.53 A/cm ²
-11	2.2	4477	68.6	6.7	6.5	
	195	6521	70.7	898		@3.53 A/cm ²
-12	2.2	4495	69.8	6.8	5.5	
	192	6523	70.6	885		@3.48 A/cm ²

Table V.— High illumination I-V data (25 °C) for 15-cell (1x1 cm) MIMs with $E_g = 0.74$ eV (Run 502).

Cell I.D.	Isc (mA)	Voc (mV)	FF (%)	Pmax (mW)	AM0 η (%)	Comments
						No ARC
502-1	2.6	4854	73.7	9.2	7.5	0.3/1.0 μm emitt/LCL
	213	6923	71.5	1055		@3.86 A/cm ²
-3	2.6	4711	68.2	8.4	6.8	
	218	6979	71.8	1091		@3.95 A/cm ²
-4	2.6	4840	73.7	9.1	7.4	
	217	6909	70.3	1095		@3.93 A/cm ²
-5	2.5	4504	73.3	8.2	6.7	
	211	6888	70.0	1018		@3.82 A/cm ²
-6	2.5	4400	68.0	7.6	6.2	
	217	6939	71.0	1069		@3.93 A/cm ²
-7	2.5	4181	71.4	7.5	6.1	
	219	6834	65.5	978		@3.97 A/cm ²
-8	2.5	4753	71.6	8.4	6.8	
	217	6889	71.4	1067		@3.93 A/cm ²
-9	2.5	4107	70.6	7.1	5.8	
	214	6828	66.5	972		@3.88 A/cm ²
-10	2.5	4301	70.3	7.5	6.1	
	220	6941	68.1	1038		@3.99 A/cm ²
-11	2.4	4380	71.6	7.5	6.1	
	206	6616	65.6	896		@3.73 A/cm ²
-12	2.4	4204	64.9	6.5	5.2	
	208	6817	68.9	976		@3.77 A/cm ²

Table VI.— High illumination I-V data (25 °C) for 15-cell (1x1 cm) MIMs with $E_g = 0.74$ eV (Run 503).

Cell I.D.	Isc (mA)	Voc (mV)	FF (%)	Pmax (mW)	AM0 η (%)	Comments
						No ARC
503-1	2.6	4936	67.8	8.7	7.1	0.3/1.0 μm emitt/LCL
	214	6962	73.9	1102		@3.88 A/cm ²
-2	2.5	4837	73.0	8.9	7.3	
	219	6938	71.4	1085		@3.97 A/cm ²
-3	2.6	4673	70.9	8.7	7.1	
	223	7059	70.7	1112		@4.04 A/cm ²
-4	2.6	4516	72.2	8.4	6.8	
	212	6802	68.1	984		@3.84 A/cm ²
-5	2.5	3813	72.0	6.9	5.6	
	213	6758	62.3	895		@3.85 A/cm ²
-6	2.6	4580	71.7	8.4	6.8	
	215	6832	71.1	1043		@3.89 A/cm ²
-7	2.6	4250	68.5	7.4	6.0	
	218	7059	69.1	1064		@3.95 A/cm ²
-8	2.5	4445	71.5	7.8	6.4	
	213	6826	67.3	977		@3.85 A/cm ²
-9	2.4	4757	73.8	8.5	6.9	
	209	6827	71.3	1020		@3.79 A/cm ²
-10	2.5	4526	71.6	8.1	6.6	
	211	6711	71.7	1014		@3.82 A/cm ²
-11	2.4	4131	68.3	6.8	5.5	
	205	6558	65.6	882		@3.72 A/cm ²
-12	2.3	4769	73.2	8.1	6.6	
	200	6837	71.4	977		@3.62 A/cm ²

Table VII.— High illumination I-V data (25 °C) for 15-cell (1x1 cm) MIMs with $E_g = 0.74$ eV (Run 499).

Cell I.D.	Isc (mA)	Voc (mV)	FF (%)	Pmax (mW)	Jsc (A/cm ²)	Comments
						No ARC
499-1	213	6576	63.5	889	3.86	0.3/1.0 μ m emit/LCL
-2	206	6678	75.1	1036	3.74	
-3	224	6687	63.9	958	3.73	
-4	183	6414	68.5	802	3.32	
-5	176	6581	70.6	818	3.19	
-6	180	6718	74.2	898	3.26	
-7	178	6683	71.1	846	3.23	
-8	177	6589	71.2	830	3.21	
-9	174	6360	70.3	779	3.15	
-10	172	6623	48.1	547	3.12	partly missing one back contact
-11	168	6384	72.2	773	3.04	
-12	166	6167	51.0	522	3.01	partly missing one back contact

Similar to what is commonly observed in other solar cells (e.g. Si, GaAs, etc.) at high illumination levels, the increase in Voc for all the devices in the above tables is an exponential function of Jsc. This is shown in Figure 12, where Voc is plotted against Jsc for a typical MIM device (Run 500).

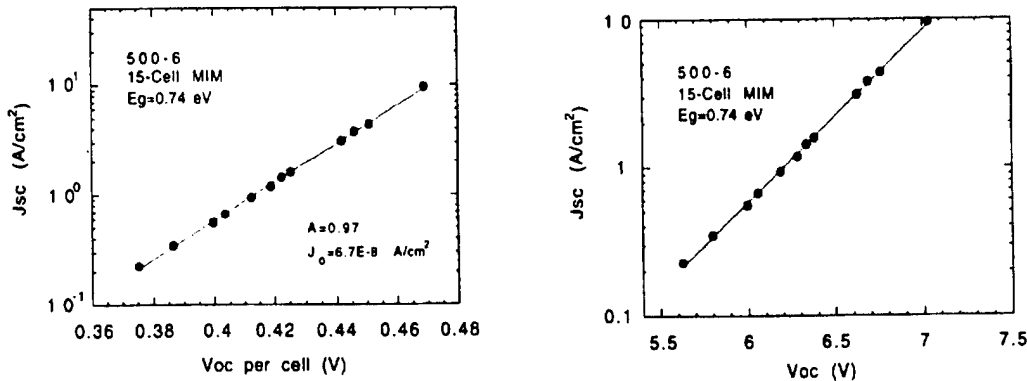


Figure 12.—Variation of Voc with Jsc for a MIM with $E_g = 0.74$ eV (logarithmic curve fit shown).

As shown in the above figures, excellent diode ideality factor (A) and reverse saturation current density (J_0) values were observed with this MIM: 0.97 and $6.7 \times 10^{-8} \text{ A/cm}^2$, respectively. The effect of the series resistance on device fill factor was determined by a plot of J_{sc} vs. FF. This data is shown for the same MIM device in Figure 13.

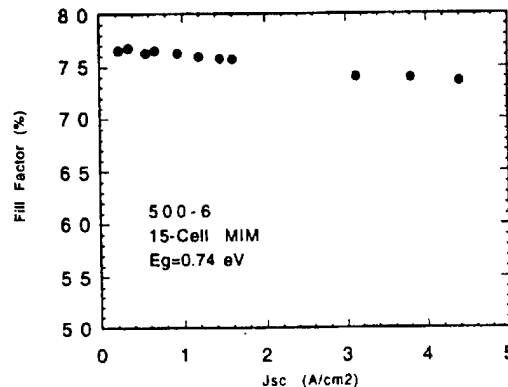


Figure 13.—Variation of the fill factor (FF) with the current density (J_{sc}) for a MIM with $E_g = 0.74 \text{ eV}$.

As shown in the figure, FF values of greater than 73% were recorded at the anticipated output J_{sc} for this MIM. This is an indication that the series resistance of the device had only a slight effect on its performance.

3.1.3. Back Surface Reflector (BSR) Reflectivity Data

MIM devices with a bandgap of 0.74 eV were tested for their IR reflectivity. A gold BSR was deposited on the bottom side of the MIMs to provide for high reflectivities. Greater reflectivities translate directly to greater optical recycling in a TPV system. As seen in Figure 14, greater than 90% of the out-of-band radiation in the wavelength range of $2\text{-}4 \mu\text{m}$ were reflected back through the MIM structure without being lost. Free carrier absorption (FCA) and plasma reflectance in the doped semiconductor layers of the MIM structure are responsible for the lower reflectivities observed in the wavelength range of $4\text{-}9 \mu\text{m}$. The overall integrated reflectivity is, however, better than what is achievable with most filters.

The thickness and doping densities in the semiconducting layers of the MIM structure can, however, be optimized to increase reflectivity in the entire out-of-band wavelengths. In fact, experiments done in the Bettis labs with more optimized MIM designs, have indicated greater than 90% reflectivity for the wavelength range of $2\text{-}15 \mu\text{m}$.

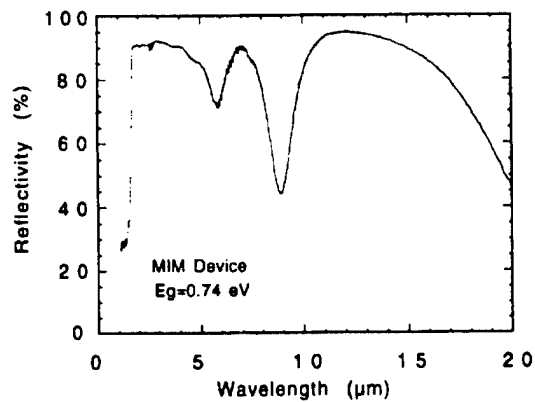


Figure 14.—Measured reflectivity data for a MIM with a gold BSR ($E_g=0.74$ eV).

3.2. MIM Array High-Level light Illumination I-V Data

The characterization and testing of the components presented in the preceding sections allowed for the performance characterization and selection of individual MIMs for the array fabrication. In this section, the performance of individual strings (1x1-cm MIMs connected in series) under LAPSS testing are presented. A photograph of two strings of MIMs on a heat-sink is shown in Figure 15.

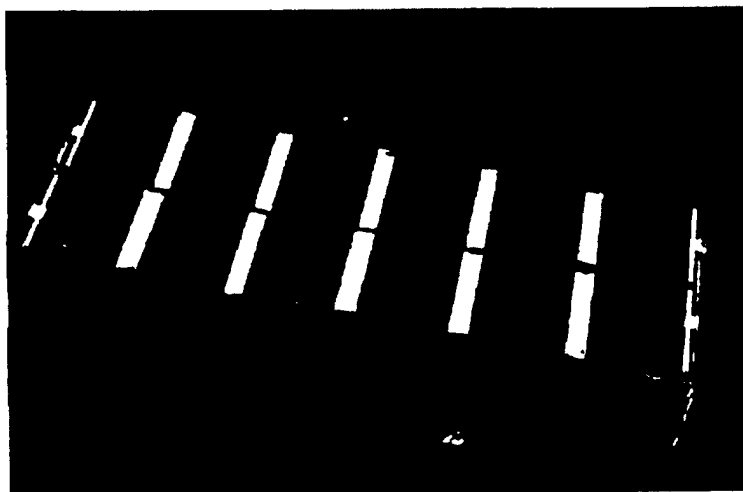


Figure 15.—A photograph of two strings of MIMs on a heat-sink.

Two strings of 1x1-cm MIMs were fabricated and tested under LAPSS. Originally, each string was composed of six MIMs. One MIM from each string was, however, damaged during assembly. These damaged MIMs were then electrically taken out of the circuit. As a result, the data presented below signifies the performance of strings with only five MIMs connected in series in each string. The V_{oc} vs. J_{sc} , FF vs. J_{sc} , and total output power (P_{out}) vs. J_{sc} , as measured with a LAPSS system, for strings #1 and #2 are presented in Figures 16-19.

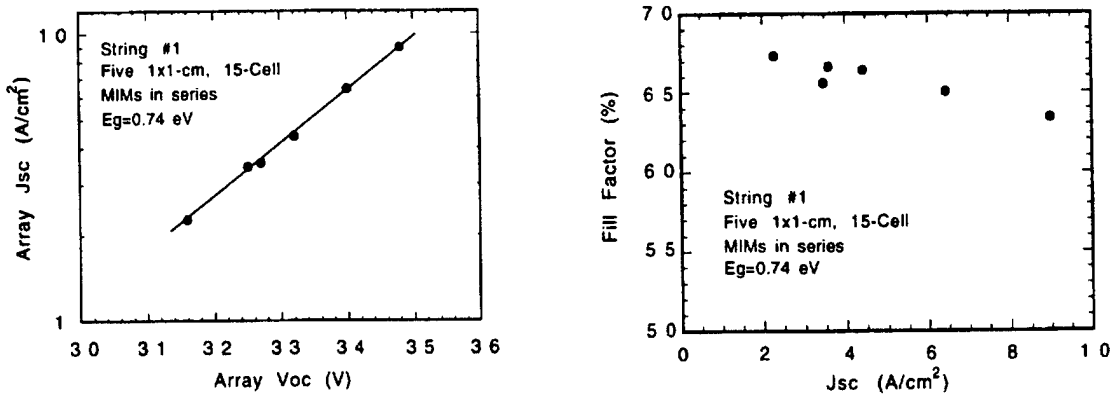


Figure 16.—Variation of Voc with Jsc (left), and Jsc with FF (right) for String #1 (LAPSS Data).

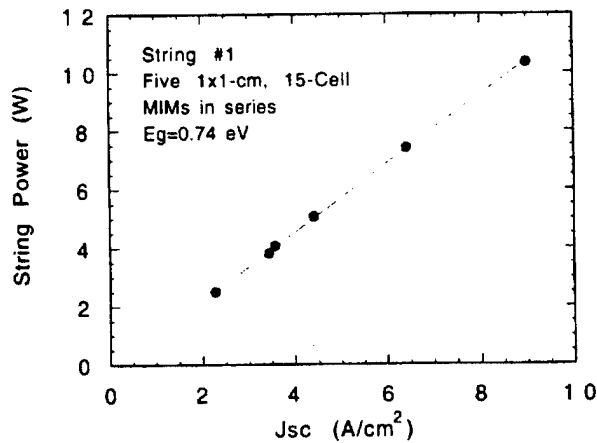


Figure 17.—Variation of output power (P_{om}) with Jsc for string #1 (LAPSS Data).

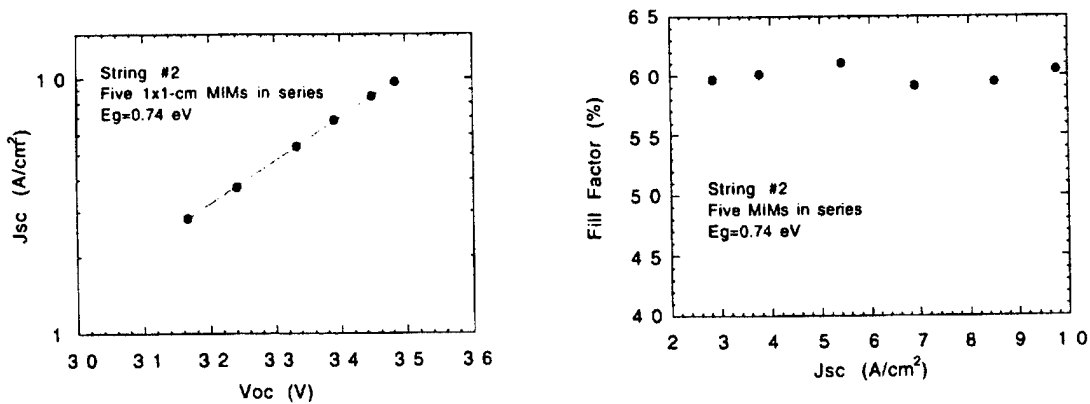


Figure 18.—Variation of Voc with Jsc (left), and Jsc with FF (right) for String #2 (LAPSS Data).

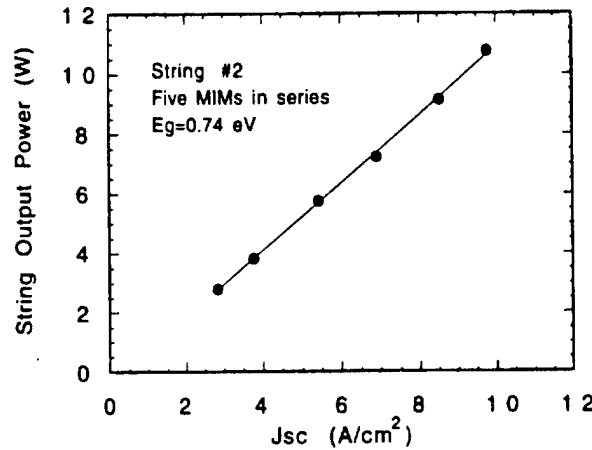


Figure 19.—Variation of output power (P_{out}) with J_{sc} for string #2 (LAPSS Data).

3.3. MIM Array Testing with the Stirling Dish Solar Concentrator

The set up procedure for this testing is described in Section 2.4. In the previous section, the performance of the MIM strings was measured with a flashlamp (*i.e.*, LAPSS) system. In this section, the performance of these strings under actual TPV conditions is presented.

During the solar testing, the SiC emitter temperature was varied from approximately 1100-1600 K. Four thermocouples (TC) were used on the four sides of the strings to measure the emitter temperature. At each test point, a maximum temperature variation (*i.e.*, non-uniformity) of less than 150°C was observed when the readings from all TCs were compared. As the SiC emitter temperature was increased, the I-V characteristics of the MIM arrays were recorded in regular intervals. As a result, electrical performance plots were generated similar to what was presented in the previous section. The V_{oc} vs. J_{sc} , FF vs. J_{sc} , and total output power (P_{out}) vs. J_{sc} , as measured under TPV conditions, for strings #1 and #2 are presented in Figures 20-23.

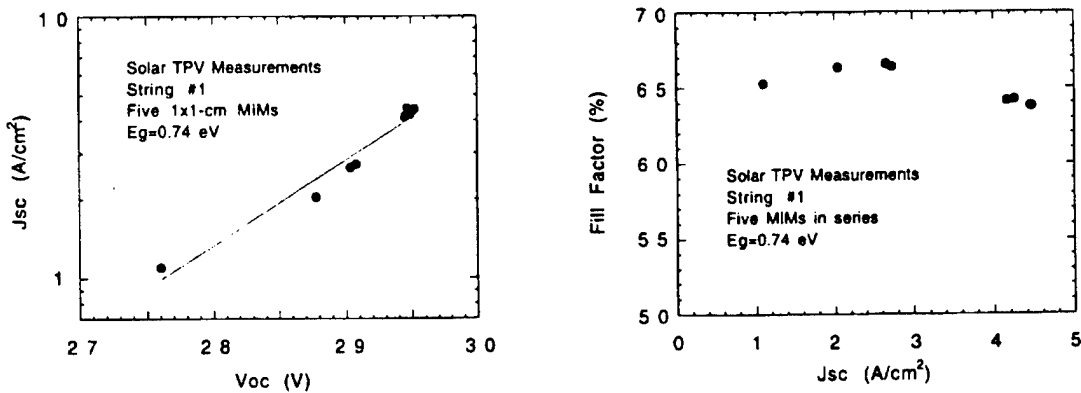


Figure 20.—Variation of V_{oc} with J_{sc} (left), and J_{sc} with FF (right) for String #1 (STPV Data).

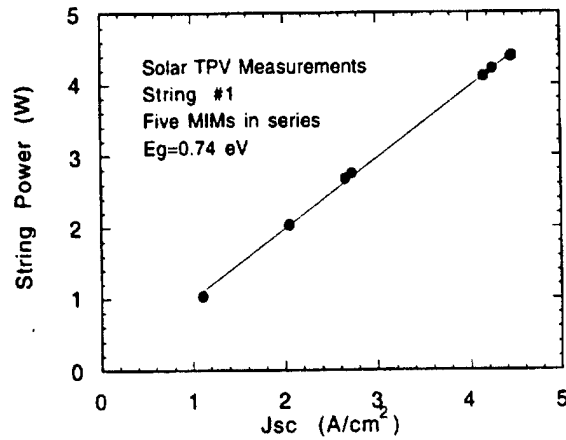


Figure 21.—Variation of output power (P_{out}) with J_{sc} for string #1 (STPV Data).

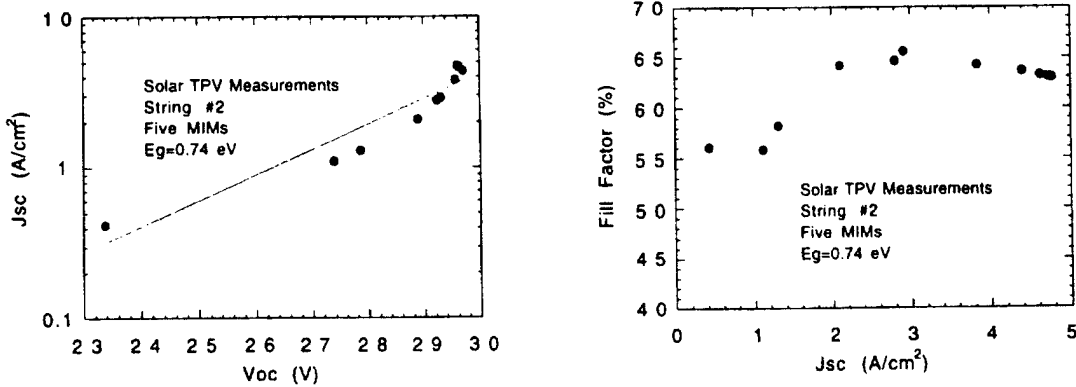


Figure 22.—Variation of V_{oc} with J_{sc} (left), and J_{sc} with FF (right) for String #2 (STPV Data).

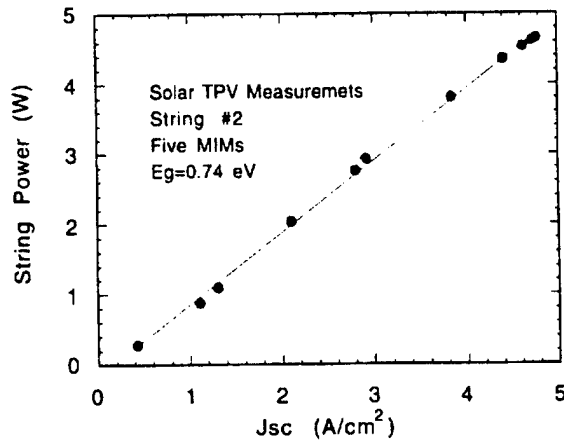


Figure 23.—Variation of output power (P_{out}) with J_{sc} for string #2 (STPV Data).

When the above J_{sc} vs. V_{oc} plots, for both MIM strings are compared with the J_{sc} vs. V_{oc} plots measured under LAPSS conditions (Section 3.1), it becomes apparent that under the actual TPV testing the V_{oc} that is measured at a given J_{sc} point is lower than what is measured under simulated flashlamp testing. We believe that this is due to the fact that the actual MIM string temperature is greater than ambient room temperature when it is placed in close proximity to the high temperature SiC emitter. As expected, this effect is more pronounced at higher J_{sc} values (*i.e.*, higher emitter temperatures) where the increase in string V_{oc} as a function of J_{sc} becomes smaller (for example, Figure 21). The fill factor values that were recorded as a function of J_{sc} during the solar TPV testing, on the other hand, were in closer agreement with the LAPSS testing (compare Figures 16 and 18 with Figures 20 and 22).

To assess the performance of the strings, it is necessary to accurately measure the temperature of the SiC emitter. As described in Section 2.3, four TCs were used to measure the emitter plate temperature on the north (N), south (S), east (E), and west (W) sides of the strings. The long dimension of the strings was oriented along the north-south direction. (See Figure 6.) The electrical performance of both strings, for an average emitter temperature of 1501 K, is given in table VIII. This average temperature was calculated by adding the four TC temperature values and dividing their sum by 4. The values for these four separately recorded temperatures are also given in the table. For comparison, the calculated electrical performance of the strings, for an emitter temperature of 1500 K, based on LAPSS and quantum efficiency data is presented in Table IX. (See Section 2.4.)

Table VIII.—Electrical performance results under solar TPV testing for strings #1 and #2 (five 1x1-cm series-connected MIMs per string) for an average emitter temperature of 1501 K.

MIM String	Electrical Performance under STPV Conditions Average Emitter T=1501 K, TC: N=1500 K, S=1456 K, E=1454 K, W=1592 K	
String #1	I _{sc} J _{sc} V _{oc} FF P _{out}	218 mA 4.16 A/cm ² 29.4 V 64.2% 4.1 W
String #2	I _{sc} J _{sc} V _{oc} FF P _{out}	242 mA 4.62 A/cm ² 29.6 V 63.3% 4.5 W

Table IX.—Electrical performance results under LAPSS testing for strings #1 and #2 (five 1x1-cm series-connected MIMs per string) for an emitter temperature of 1500 K.

MIM String	Electrical Performance from LAPSS & QE Data Emitter T=1500 K	
String #1	Isc	173 mA
	Jsc	3.30 A/cm ²
	Voc	32.4 V
	FF	65.6%
	P _{out}	3.7 W
String #2	Isc	173 mA
	Jsc	3.30 A/cm ²
	Voc	32.0 V
	FF	60.0%
	P _{out}	3.3 W

As shown in Table VIII, at an average emitter temperature of 1500 K, an output power in the range of 4.1-4.5 watts is observed from each string. This translates to an output power density of 0.82-0.90 W/cm². The calculated electrical performance, shown in table IX, however shows lower output power density values: 0.66-0.74 W/cm². We conjecture that the actual average SiC emitter temperature facing the strings may have been somewhat greater than the calculated mathematical average temperature of 1501 K. This can explain the larger Jsc values observed in the solar versus LAPSS testing.

The results in the above tables show that relatively large output power densities can be obtained for the moderate emitter temperature of about 1500 K, using the proposed MIM device technology and a solar concentrator dish TPV system.

3.4. Large-Area MIM Performance Results

LAPSS testing was performed on 2x2-cm MIMs. From these measurements, diode ideality factor (A), reverse saturation current density (J₀), and the effects of the series resistance on device FF were determined. The light concentration levels were chosen such that the Jsc of each device would be in the same range as the anticipated Jsc when operating under TPV conditions. The results for some of the measurements are shown in Table X.

Table X.—High illumination I-V data (25°C) for 30-cell (2x2-cm) MIMs with Eg = 0.74 eV.

Cell I.D.	Isc (mA)	Voc (V)	FF (%)	Pmax (W)	Jsc (A/cm ²)	Comments
						0.3/1.0 μm emit/LCL
469-1	431	14.4	66.3	4.1	3.9	
504-A	430	13.0	59.8	3.3	3.9	
507-A	423	13.6	64.6	3.7	3.8	
508-A	414	13.7	62.8	3.6	3.8	
509-A	399	13.6	66.1	3.6	3.6	

The Voc vs. Jsc and Jsc vs. FF plots for device 469-1 in Table X are shown in Figure 24.

When the above J_{sc} vs. V_{oc} plots, for both MIM strings are compared with the J_{sc} vs. V_{oc} plots measured under LAPSS conditions (Section 3.1), it becomes apparent that under the actual TPV testing the V_{oc} that is measured at a given J_{sc} point is lower than what is measured under simulated flashlamp testing. We believe that this is due to the fact that the actual MIM string temperature is greater than ambient room temperature when it is placed in close proximity to the high temperature SiC emitter. As expected, this effect is more pronounced at higher J_{sc} values (*i.e.*, higher emitter temperatures) where the increase in string V_{oc} as a function of J_{sc} becomes smaller (for example, Figure 21). The fill factor values that were recorded as a function of J_{sc} during the solar TPV testing, on the other hand, were in closer agreement with the LAPSS testing (compare Figures 16 and 18 with Figures 20 and 22).

To assess the performance of the strings, it is necessary to accurately measure the temperature of the SiC emitter. As described in Section 2.3, four TCs were used to measure the emitter plate temperature on the north (N), south (S), east (E), and west (W) sides of the strings. The long dimension of the strings was oriented along the north-south direction. (See Figure 6.) The electrical performance of both strings, for an average emitter temperature of 1501 K, is given in table VIII. This average temperature was calculated by adding the four TC temperature values and dividing their sum by 4. The values for these four separately recorded temperatures are also given in the table. For comparison, the calculated electrical performance of the strings, for an emitter temperature of 1500 K, based on LAPSS and quantum efficiency data is presented in Table IX. (See Section 2.4.)

Table VIII.—Electrical performance results under solar TPV testing for strings #1 and #2 (five 1x1-cm series-connected MIMs per string) for an average emitter temperature of 1501 K.

MIM String	Electrical Performance under STPV Conditions Average Emitter T=1501 K, TC: N=1500 K, S=1456 K, E=1454 K, W=1592 K	
String #1	I _{sc} J _{sc} V _{oc} FF P _{out}	218 mA 4.16 A/cm ² 29.4 V 64.2% 4.1 W
String #2	I _{sc} J _{sc} V _{oc} FF P _{out}	242 mA 4.62 A/cm ² 29.6 V 63.3% 4.5 W

Table IX.—Electrical performance results under LAPSS testing for strings #1 and #2 (five 1x1-cm series-connected MIMs per string) for an emitter temperature of 1500 K.

MIM String	Electrical Performance from LAPSS & QE Data Emitter T=1500 K	
String #1	Isc	173 mA
	Jsc	3.30 A/cm ²
	Voc	32.4 V
	FF	65.6%
	P _{out}	3.7 W
String #2	Isc	173 mA
	Jsc	3.30 A/cm ²
	Voc	32.0 V
	FF	60.0%
	P _{out}	3.3 W

As shown in Table VIII, at an average emitter temperature of 1500 K, an output power in the range of 4.1-4.5 watts is observed from each string. This translates to an output power density of 0.82-0.90 W/cm². The calculated electrical performance, shown in table IX, however shows lower output power density values: 0.66-0.74 W/cm². We conjecture that the actual average SiC emitter temperature facing the strings may have been somewhat greater than the calculated mathematical average temperature of 1501 K. This can explain the larger Jsc values observed in the solar versus LAPSS testing.

The results in the above tables show that relatively large output power densities can be obtained for the moderate emitter temperature of about 1500 K, using the proposed MIM device technology and a solar concentrator dish TPV system.

3.4. Large-Area MIM Performance Results

LAPSS testing was performed on 2x2-cm MIMs. From these measurements, diode ideality factor (A), reverse saturation current density (J₀), and the effects of the series resistance on device FF were determined. The light concentration levels were chosen such that the Jsc of each device would be in the same range as the anticipated Jsc when operating under TPV conditions. The results for some of the measurements are shown in Table X.

Table X.—High illumination I-V data (25°C) for 30-cell (2x2-cm) MIMs with E_g = 0.74 eV.

Cell I.D.	Isc (mA)	Voc (V)	FF (%)	Pmax (W)	Jsc (A/cm ²)	Comments
						0.3/1.0 μm emit/LCL
469-1	431	14.4	66.3	4.1	3.9	
504-A	430	13.0	59.8	3.3	3.9	
507-A	423	13.6	64.6	3.7	3.8	
508-A	414	13.7	62.8	3.6	3.8	
509-A	399	13.6	66.1	3.6	3.6	

The Voc vs. Jsc and Jsc vs. FF plots for device 469-1 in Table X are shown in Figure 24.

REPORT DOCUMENTATION PAGE

Form Approved
OMB No. 0704-0188

No
SBIR
#

Public reporting burden for this collection of information is estimated to average 1 hour per response, including the time for reviewing instructions, searching existing data sources, gathering and maintaining the data needed, and completing and reviewing the collection of information. Send comments regarding this burden estimate or any other aspect of this collection of information, including suggestions for reducing this burden, to Washington Headquarters Services, Directorate for Information Operations and Reports, 1215 Jefferson Davis Highway, Suite 1204, Arlington, VA 22202-4302, and to the Office of Management and Budget, Paperwork Reduction Project (0704-0188), Washington, DC 20503.

1. AGENCY USE ONLY (Leave blank)	2. REPORT DATE December 5, 1998	3. REPORT TYPE AND DATES COVERED FINAL Contractor Report Dec. 1996—Dec. 1998	
4. TITLE AND SUBTITLE A Solar Thermophotovoltaic Electric Generator for Remote Power Applications		5. FUNDING NUMBERS C-NAS3-97047 BMD0-95-005	
6. AUTHOR(S) Navid S. Fatemi		8. PERFORMING ORGANIZATION REPORT NUMBER NAS3-97047-98F	
7. PERFORMING ORGANIZATION NAME(S) AND ADDRESS(ES) Essential research, Inc. 23811 Chagrin Blvd. Suite 280 Cleveland, OH 44122		10. SPONSORING/MONITORING AGENCY REPORT NUMBER	
9. SPONSORING/MONITORING AGENCY NAME(S) AND ADDRESS(ES) National Aeronautics and Space Administration Lewis Research Center Cleveland, Ohio 44135-3191		11. SUPPLEMENTARY NOTES	
12a. DISTRIBUTION AVAILABILITY STATEMENT Unclassified - Unlimited		12b. DISTRIBUTION CODE	
13. ABSTRACT (Maximum 200 words) We have successfully demonstrated that a solar thermophotovoltaic (TPV) system with a SiC graybody emitter and the monolithic interconnected module device technology can be realized. A custom-designed solar cavity was made to house the SiC emitter and the MIM strings for testing in a Stirling dish solar concentrator. Five 1x1-cm MIMs, with a bandgap of 0.74 eV, were mounted on a specially designed water-cooled heatsink and were electrically connected in series to form a string. Two such strings were fabricated and tested, as well as high-performance 2x2-cm MIMs with a bandgap of 0.74 eV. Very high output power density values between 0.82 and 0.90 W/cm ² were observed for an average emitter temperature of 1501 K.			
14. SUBJECT TERMS Space power; Thermophotovoltaics; Solar concentrators; InGaAs		15. NUMBER OF PAGES 31	
17. SECURITY CLASSIFICATION OF REPORT Unclassified		16. PRICE CODE	
18. SECURITY CLASSIFICATION OF THIS PAGE Unclassified	19. SECURITY CLASSIFICATION OF ABSTRACT Unclassified	20. LIMITATION OF ABSTRACT	